




## Article

# Influence of the Valence of Iron on the NO Reduction by CO over Cu-Fe-Mordenite

Yulia Kotolevich <sup>1</sup> , Trino Zepeda-Partida <sup>1</sup>, Rosario Yocupicio-Gaxiola <sup>1,2</sup>, Joel Antúnez-García <sup>1</sup> , Luis Pelaez <sup>3</sup>, Miguel Avalos-Borja <sup>4</sup>, Pedro Jovanni Vázquez-Salas <sup>1</sup>, Sergio Fuentes-Moyado <sup>1</sup> and Vitalii Petranovskii <sup>1,\*</sup> 

<sup>1</sup> Centro de Nanociencias y Nanotecnología, Universidad Nacional Autónoma de México, Ensenada 22860, Mexico

<sup>2</sup> Instituto Tecnológico Superior de Guasave, Ejido Burroncito 81149, Mexico

<sup>3</sup> Fleet Complete, Variable Capital Limited Liability Company, México City 11320, Mexico

<sup>4</sup> División de Materiales Avanzados, Instituto Potosino de Investigación Científica y Tecnológica, San Luis Potosí 78216, Mexico

\* Correspondence: vitalii@ens.cnyn.unam.mx

**Abstract:** A comprehensive study of the catalytic properties of the copper-iron binary system supported on mordenite, depending on the iron valence—CuFe<sub>2</sub>MOR and CuFe<sub>3</sub>MOR—was carried out, and redox ability has been considered as a decisive factor in determining catalytic efficiency. Acidity was studied by TPD-NH<sub>3</sub>, DRIFT-OH, and DRT methods. The total acidity of both samples was high. The Brønsted acidity is similar for both bimetallic samples and is explained by the acidity of zeolite; Lewis acidity varies greatly and depends on the exchange cations. A screening DRIFT study of CO and NO has shown redox capacity and demonstrated a potential for using these materials as catalysts for ambient protection. CuFe<sub>2</sub>MOR demonstrated stable Cu and Fe species, while CuFe<sub>3</sub>MOR showed redox dynamic species. As expected, CuFe<sub>3</sub>MOR displayed higher catalytic performance in NO reduction via CO oxidation, because of the easily reduced intermediate NO-complex adsorbed on the metallic Cu and Fe sites, which were observed through in situ DRIFT study.

**Keywords:** mordenite; ion exchange; copper; iron (II); iron (III); surface acidity; DRIFT in situ



**Citation:** Kotolevich, Y.; Zepeda-Partida, T.; Yocupicio-Gaxiola, R.; Antúnez-García, J.; Pelaez, L.; Avalos-Borja, M.; Vázquez-Salas, P.J.; Fuentes-Moyado, S.; Petranovskii, V. Influence of the Valence of Iron on the NO Reduction by CO over Cu-Fe-Mordenite. *Catalysts* **2023**, *13*, 484. <https://doi.org/10.3390/catal13030484>

Academic Editors: Farid Orudzhev and Irina A. Zvereva

Received: 27 January 2023

Revised: 19 February 2023

Accepted: 23 February 2023

Published: 27 February 2023



**Copyright:** © 2023 by the authors. Licensee MDPI, Basel, Switzerland. This article is an open access article distributed under the terms and conditions of the Creative Commons Attribution (CC BY) license (<https://creativecommons.org/licenses/by/4.0/>).

## 1. Introduction

Various catalytic technologies have been developed to remove pollutants from engine exhaust gases. In this study, a three-way catalyst (TWC) for emissions from combustion engines is designed to remove hydrocarbons (HC), carbon monoxide, and nitrogen oxides (NO<sub>x</sub>) from a stoichiometric gas mixture [1]. The majority of automotive catalytic converters have a monolithic structure, which is coated with an alumina washcoat on which noble metals such as platinum, palladium, and rhodium are deposited [2]. Due to tighter pollution requirements, skyrocketing prices for platinum group metals, and a concomitant growing car fleet, several proposals have been made in recent years to upgrade these catalysts, mainly with the aim of replacing precious metals with cheaper and more common elements. As a rule, excellent redox properties and strong acidity are two decisive factors in determining catalytic efficiency. The redox ability inherent in metal species mainly catalyzes the redox cycle, while the work of acid sites is to facilitate the adsorption and activation of reactant molecules and is mainly provided by the support.

The most promising supports in this sense are zeolites. They are characterized by a large specific surface area and high ion-exchange capacity, which provides a wide range of type and content of loaded metals; and the ability to change the composition of the zeolite matrix (the atomic ratio of Cu/Al, and heteroatoms embedded in the framework by isomorphic substitution) provides significant variations in acidity, which generally creates a wide-ranging choice of possible composition and, accordingly, properties of the catalyst. By controlling the Si/Al ratio, a desirable surface acidity can be obtained over a wide operating temperature range. The unique and uniform size and structure of the pores created by

the crystal structure provide selectivity in the size and shape of the reacting molecules. However, zeolite catalysts still face many challenges associated with the development of multicomponent composite materials [3,4].

In terms of active metal, the best choice is a transition metal with a redox potential and self-regeneration ability, which is most likely to be achieved in a polymetallic system. In this paper, we consider the Cu-Fe bimetallic system, using iron salts in both the two- and three-valent state for the preparation of samples. Both metals have a low cost compared to noble metals and high selectivity, and are more stable compared to oxide catalysts. In accordance with the recent literature data, both Cu- and Fe-zeolite catalysts exhibit catalytic activity in all three reactions required for TWC: the oxidation of CO [5], deNO<sub>x</sub> by NH<sub>3</sub> or hydrocarbons [6–10], and the oxidation of hydrocarbons [11].

The aim of this work is to study the effect of iron valence in the initial reagents on the acidity, adsorption, and catalytic properties of the bimetallic mordenite-based catalysts CuFe2MOR and CuFe3MOR.

## 2. Results and Discussion

Copper(II), iron(II), and iron(III), individually or in combination, were deposited by ion exchange of mordenite on a sodium form (NaMOR) with an atomic ratio of Si/Al = 6.5 (for details see Section 3). The samples were labeled as CuMOR, FeNMOR, and CuFeNMOR, where *N* = 2 or 3 and corresponds to the oxidation degree of iron in the precursor solution (Fe<sup>2+</sup> or Fe<sup>3+</sup>, respectively). After the ion exchange procedure, the samples were reduced at 350 °C for 1 h in a hydrogen flow.

### 2.1. X-ray Diffraction Studies and Chemical Composition

X-ray diffraction (XRD) analysis of the initial sample and the prepared materials after the deposition of iron and copper in various combinations confirmed that all samples retain their original mordenite crystalline structure. The crystalline phases were identified using the Joint Committee Powder Diffraction Standards (JCPDS) files (file 43-0171 corresponds to mordenite). Figure 1 shows X-ray diffraction patterns of the original NaMOR and all of the ion-exchanged samples (CuMOR, Fe2MOR, Fe3MOR, CuFe2MOR, and CuFe3MOR). As can be seen, all peaks of the crystal structure of NaMOR are retained after the exchange of Na for Cu and/or Fe ions. It should be noted that variations in the relative intensities of several peaks which are sensitive to the incorporation of exchanged Fe ions were considered in our previous article [2].

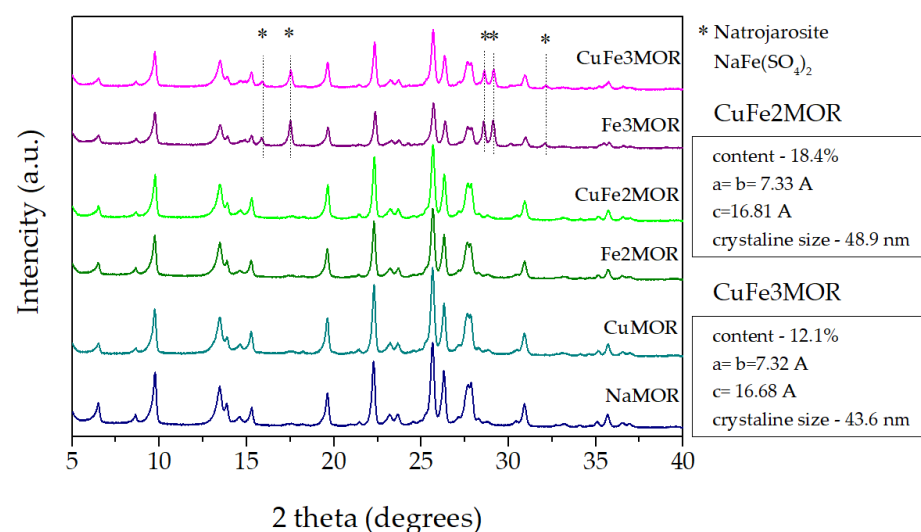


**Figure 1.** Powder XRD patterns for the studied samples. Stars indicate diffraction peaks corresponding to Natrojarosite.

It is important to note that, in addition to the peaks of mordenite itself, the X-ray diffraction patterns of Fe3MOR and CuFe3MOR samples prepared using iron(III) solutions show additional peaks (see Figure 1) that may correspond to natrojarosite ( $\text{NaFe}_3(\text{SO}_4)_2(\text{OH})_6$ , Card # 00-011-0302, Reference code 00-036-0425). According to the results of the phase analysis, the proportion of natrojarosite was 18.4 and 12.1 wt% for the Fe3MOR and CuFe3MOR samples, respectively. Similar to alum, natrojarosite is a double sulfate of the mono- and tri-valent metals,  $\text{Na}^+$  and  $\text{Fe}^{3+}$ , and belongs to the alunite supergroup of minerals [12]. Such compounds are widely distributed in nature. Interestingly, this is not the first observation of the formation of such an admixed sulfate phase during ion exchange using microwave radiation. Previously, in the preparation of copper-exchanged mordenite, the formation of an epitaxially growing impurity antlerite phase  $\text{Cu}_3(\text{OH})_4\text{SO}_4$  (up to 6 wt%) was observed during ion-exchange treatment under microwave irradiation [13,14]. This means that, although the ion exchange procedure with MW stimulation leads to a deeper exchange compared to the traditional procedure, an additional amount of metal ions may be consumed to form a new impurity phase. Thus, the synthesis with the participation of MW, which is becoming increasingly popular as it is fast and inexpensive, can not only enhance the ion exchange, but also be accompanied by side chemical reactions. These phenomena, both observed previously [14] and found in this study, may not be unique, but common, and should be taken into account.

Changes in the general character of XRD patterns were not observed; there is no change in the half-widths of the peaks, i.e., there was no deterioration in the crystallinity of the lattice. The lattice parameters of mordenite before and after ion exchange are shown in Table 1. Parameter  $c$  is almost constant for the entire set of samples; parameters  $a$  and  $b$  show more significant changes. Parameter  $b$  has a maximum value for the initial NaMOR support and decreases with any of the ion exchanges. All three parameters of samples with  $\text{Fe}^{3+}$  have close values, differing more noticeably from other samples. Parameter  $a$  has maximum values for Fe2MOR and CuMOR; however, after exchange with  $\text{Cu}^{2+}$  in the bimetallic CuFe2MOR sample, this parameter displayed a minimal value for the entire series. Note that Fe3MOR and CuFe3MOR have an equal value for parameter  $a$ . This means that  $\text{Fe}^{2+}$  and  $\text{Fe}^{3+}$  interact with different mordenite centers.

**Table 1.** Lattice parameters of mordenite before and after ion exchange.

Sample	$a$	$b$	$c$	$K = a/b$
NaMOR	18.12	20.46	7.51	0.886
CuMOR	18.15	20.42	7.51	0.889
Fe2MOR	18.16	20.43	7.51	0.889
CuFe2MOR	18.11	20.41	7.51	0.887
Fe3MOR	18.14	20.36	7.50	0.891
CuFe3MOR	18.14	20.37	7.50	0.891

The main channels in the structure of mordenite are directed along the  $c$  axis. Due to the small difference between the axes  $a$  and  $b$  in the unit cell of mordenite, the channel has an elliptical cross section. The ellipticity parameter  $K$ , chosen as the ratio  $a/b$ , can be calculated and has a certain character. It was shown earlier in [15], for monometallic Cu-Mordenite series, that  $K$  increases with an increasing copper concentration. In our case, bimetallic systems were studied, and the  $K$  dependence was not so obvious. However, note that the contraction-expansion of the channel and the change in ellipticity during ion exchange is due to the influence of ion-exchange cations; therefore, this means that they are in the channel of the zeolite, and not on the surface of the zeolite.

The chemical composition of the samples was determined by the method of Inductively Coupled Plasma–Optical Emission Spectroscopy (ICP–OES). The results of the analyses are presented in Table 2. It is known that cations in the zeolite framework compensate for the negative charge in the lattice; therefore, their content should correspond to the amount of aluminum in the structure [16] and, accordingly, the caustic modulus (equal to the  $\text{Na}/\text{Al}$

ratio) should be equal to the unity. However, the initial commercial zeolite in the sodium form has a sufficiently higher caustic modulus. Apparently, excess  $\text{Na}^+$  is occluded in the pore space, probably due to insufficient washing of the commercial mordenite at the production stage [17–20]. During the ion-exchange procedure, in addition to the exchange of  $\text{Na}^+$  ions, excess of  $\text{Na}^+$  content is removed by washing with aqueous precursor solutions. In this case, only those cations that compensate for the negative charge in the zeolite lattice remain in the composition of the sample, and the sum of their positive charges divided by the aluminum content can be called the Equilibrium Ion-Exchange Modulus (EIEM); it must be equal to one [16]. In this study, the compensatory cations are  $\text{Cu}^{2+}$ ,  $\text{Fe}^{2+}$ ,  $\text{Fe}^{3+}$ , and  $\text{H}^+$  (from  $\text{H}_2\text{SO}_4$ ), along with the residual part of  $\text{Na}^+$  (if any). It is important to note that it is impossible to estimate the content of  $\text{H}^+$  using the ICP-OES method. Thus, in our case,

$$\text{EIEM} = \frac{\text{Na}}{\text{Al}} + \frac{\text{Cu}}{2 \cdot \text{Al}} + \frac{\text{Fe}}{n \cdot \text{Al}}, \quad (1)$$

where  $n = 2$  or  $3$  is the charge of the  $\text{Fe}^{n+}$  cation.

**Table 2.** Element composition and EIEM for the studied samples determined by ICP-OES.

Sample	Si	Al	Si/Al	Na	Cu	Fe	EIEM
NaMOR	40.04	6.12	6.55	7.00	-	-	1.14
CuMOR	38.97	5.88	6.62	3.34	1.41	-	1.05
Fe2MOR	41.80	6.19	6.75	3.82	-	1.18	0.71
CuFe2MOR	41.10	6.00	6.85	3.82	0.85	0.62	0.74
Fe3MOR	35.40	4.10	8.63	3.82	-	3.26	1.20
CuFe3MOR	36.82	4.79	7.68	3.63	0.88	1.81	0.98

Considering the acid treatment of most samples, it should be noted that, for samples with ferrous iron, the Si/Al ratio of the initial mordenite does not change significantly. A slight dealumination was observed, in which the Si/Al ratio increased from 6.55 to 6.85. In the case of the samples with ferric iron, Fe3MOR and CuFe3MOR, the dealumination is much larger and, given the results for Fe(II), cannot be related only to the acid treatment used. Note that the amount of Fe in samples containing  $\text{Fe}^{3+}$  is much higher than in samples containing  $\text{Fe}^{2+}$ . XRD data have already confirmed that part of the iron is spent on the formation of an impurity phase of natrojarosite  $\text{NaFe}(\text{SO}_4)_2$ . In addition, it can be assumed that  $\text{Fe}^{3+}$  ions participate not only in ion exchange and lateral chemical reaction, but can also partially replace Al cations in the mordenite crystal framework, similar to the process observed for the AgFeMOR binary system [21].

## 2.2. Morphology and Textural Studies

The below high resolution transmission electron microscopy (HRTEM) images (see Figure 2a–c) demonstrate the formation of nanoparticles in all of the samples containing copper. Based on the micrographs for all three samples, the particle size distribution was determined, and the histograms are presented in Figure 2d–f. As can be seen, the distribution is bimodal; for CuMOR and CuFe3MOR, the maxima are 2 and 5 nm, and the maximum at 2 nm is 2–3 times higher than the second one. In the case of CuFe2MOR, the distribution is wider, and both maxima are shifted towards larger sizes and are observed at 4 and 8 nm; note that they are relatively close in their intensity. Since the XRD data (see Figure 1) did not demonstrate any metal or oxide phase of Cu, it might be some non-structural copper species. This could mean that applied composition and the method of synthesis lead to a diversity of copper species, which might affect its catalytic performance.

The textural properties of the studied samples, presented in Table 3, did not undergo significant changes compared to the original NaMOR. The  $\text{N}_2$  adsorption/desorption isotherms for all samples are shown in Figure S1 in Supplementary Materials. In the presence of Cu, the specific surface area and pore diameter slightly increase; this may be due to the removal of occluded Na compounds.



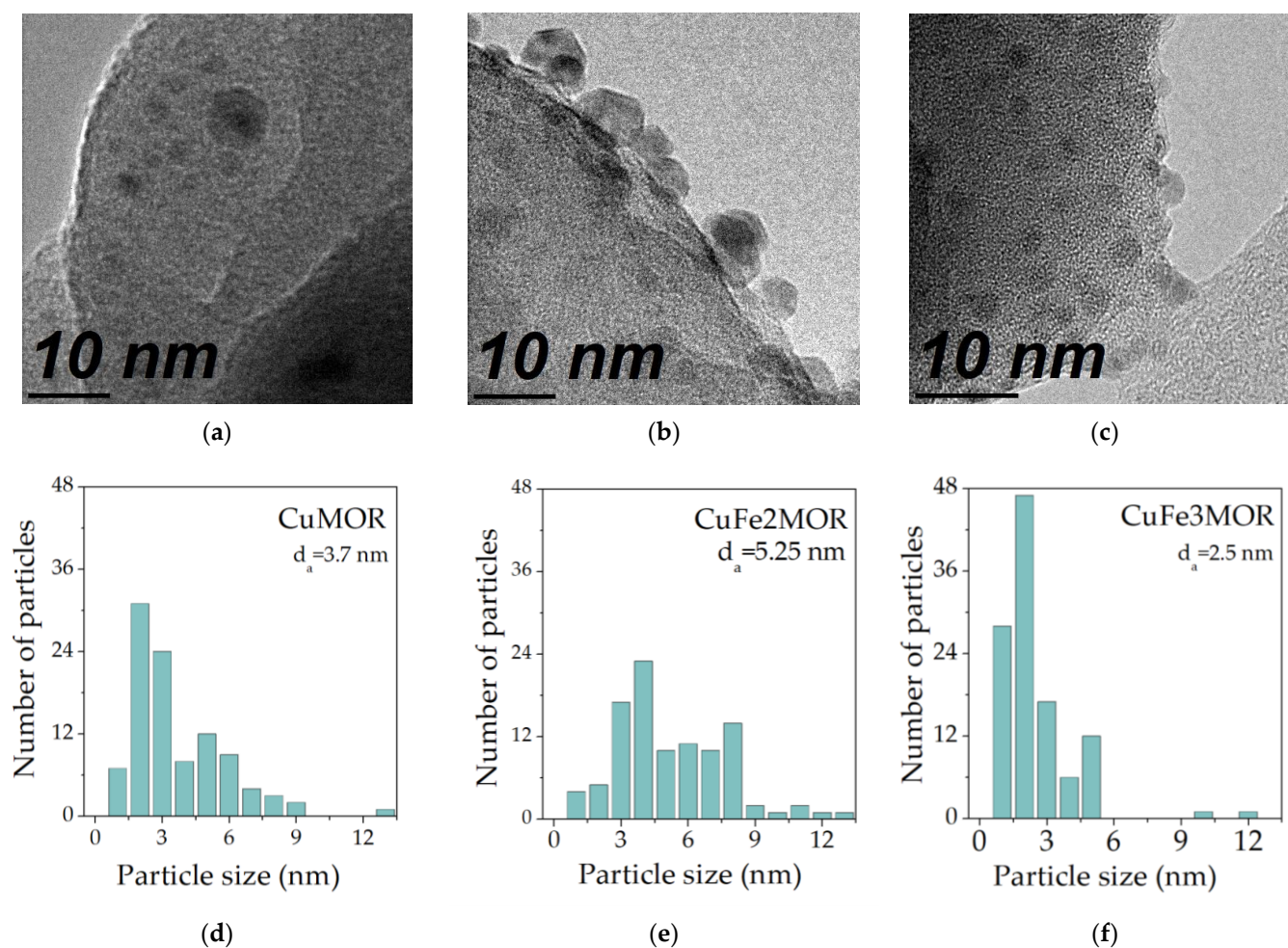


**Figure 2.** HRTEM images and particle size distribution of studied samples.

**Table 3.** Textural properties of studied samples.

Sample	$S_{BET}$ , $m^2 \cdot g^{-1}$	$V_{total}$ , $cm^3 \cdot g^{-1}$	$d$ , Å
NaMOR	297	0.04	170
CuMOR	309	0.04	360
Fe2MOR	275	0.04	201
CuFe2MOR	313	0.05	379
Fe3MOR	288	0.05	171
CuFe3MOR	302	0.04	346

### 2.3. Surface Acidity

Temperature-Programmed Desorption of Ammonia (TPD-NH<sub>3</sub>) is one of the most common methods for characterizing the total Lewis acidity in zeolites. The amount of ammonia desorbed over a given temperature range is taken as a measure of the acid site concentration, whereas the temperature ranges at which most of the ammonia is desorbed indicate the acid strength distribution. All of the studied samples demonstrated desorption of ammonia in the form of three peaks. The experimental low-temperature peak (below 200 °C) is assigned to NH<sub>3</sub> desorption from Lewis acid sites together with NH<sub>3</sub> desorption from a [Cu(II)(OH)(NH<sub>3</sub>)<sub>3</sub>]<sup>+</sup> complex [22]. It is also possible that the auto-reduction of Cu<sup>2+</sup> to Cu<sup>+</sup> occurred during the activation step in vacuum, inducing true Lewis acid sites [23]. The mid-temperature peak (250–350 °C) is attributed to the decomposition of a linear [Cu(I)(NH<sub>3</sub>)<sub>2</sub>]<sup>+</sup> complex and a residual from [Cu(II)(OH)(NH<sub>3</sub>)<sub>3</sub>]<sup>+</sup>. The high-temperature peak is predicted to have contributions from Brönsted acid sites (NH<sub>4</sub><sup>+</sup>), [Cu(I)NH<sub>3</sub>]<sup>+</sup>, and [Cu(II)(NH<sub>3</sub>)<sub>4</sub>]<sup>2+</sup> [22].

The results of the  $\text{NH}_3$ -TPD experiments for Fe- and Cu-exchanged zeolites, carried out on a microbalance, are reported in Table 4. The initial mordenite presents a homogeneous strength distribution of all acid sites, while a heterogeneous strength distribution is observed for all exchanged samples. The initial zeolite is characterized by only weak acidity centers. Ion exchange increases the strength of acid sites; however, all samples demonstrate predominantly weak acidity (64–74%). In second place are centers of medium acidity (13–26%), and in the smallest amount—strong ones (8–22%). Note that the exchange for Cu and  $\text{Fe}^{2+}$  increases the strength of acid centers and the total acidity, while, in the presence of  $\text{Fe}^{3+}$ , they decrease. This causes bimetallic materials to exhibit the effects of interaction between both metals and support. CuFe2MOR has the strongest surface acidity and the highest total acidity. These results will be compared with DRIFT spectra of the hydroxyl region and a theoretical study by DFT.

**Table 4.** Acidity by TPD  $\text{NH}_3$ .

Sample	Amount of Acid Sites			Total Acidity, mmol/g
	Weak, %	Medium, %	Strong, %	
NaMOR	100.0	0.0	0.0	1439
CuMOR	70.7	16.1	13.2	2108
Fe2MOR	74.3	17.4	8.3	1732
CuFe2MOR	43.0	34.9	22.2	2991
Fe3MOR	64.4	25.8	9.9	1218
CuFe3MOR	66.9	12.7	20.4	1653

For the target bimetallic materials, CuFe2MOR and CuFe3MOR, a detailed study of acidity was carried out using Diffuse Reflectance Infrared Fourier Transform spectroscopy (DRIFT) of OH stretching vibration (Figure 3). As can be seen, both samples demonstrate the same peaks, and in the case of CuFe2MOR, they are somewhat more intense than in the case of CuFe3MOR. It has been reported that typical Brönsted OH stretching values, due to acidic protons, can be in the range from 3650 to 3550  $\text{cm}^{-1}$ , while values assigned to silanol groups can be found at 3750  $\text{cm}^{-1}$  [24]. In this sense, the appearance of a band at 3750  $\text{cm}^{-1}$  reveals the stretching vibrations of terminal silanol groups [25]. On the other hand, for the OH stretching of the Brönsted acid sites, several different contributions can be seen, located at 3650, 3630, and 3615  $\text{cm}^{-1}$ . The signal at 3615  $\text{cm}^{-1}$  can be assigned to the stretching vibration that is typical for -OH groups, which is located in the main channels [26], while the signal at 3630  $\text{cm}^{-1}$  can be attributed to OH stretching vibrations in close interaction with the probe molecule [27], while the presence of this band had been attributed to the presence of structural iron in the form of  $\text{Si}(\text{OH})\text{Fe}$  groups [28]. The presence of a shoulder at 3670  $\text{cm}^{-1}$  can be associated with the presence of OH linked to extra framework Al, which are partially linked to the framework [29]. The nature and mechanism of formation during the ion exchange of these Al centers, which are absent in the original carrier, is of particular interest; however, its study is beyond the task set out in this work. Definitely, both studied samples represent a significant contribution of Brönsted acid sites, as evidenced by the analysis of the OH region.

In the present work, we considered a model of mordenite zeolite with a Si/Al = 7 ratio ( $6\text{Na}^+[\text{Al}_6\text{Si}_{42}\text{O}_{96}]^{6-}$ ), which is close to the experimental value shown for NaMOR in Table 2, and which was recently reported in [30]. Based on this model, we searched for the most energetically favorable site for the ionic substitution of Na for Fe. Once this position was determined, we included Cu in the calculations. For this second inclusion, we then looked for the most energetically favorable site for the ionic substitution of Na for Cu. It is worth mentioning that we also investigated the reverse process: Cu was introduced first, and then Fe. Various configurations were optimized through periodic DFT calculations, following the same procedure and parameterization described earlier in [30].

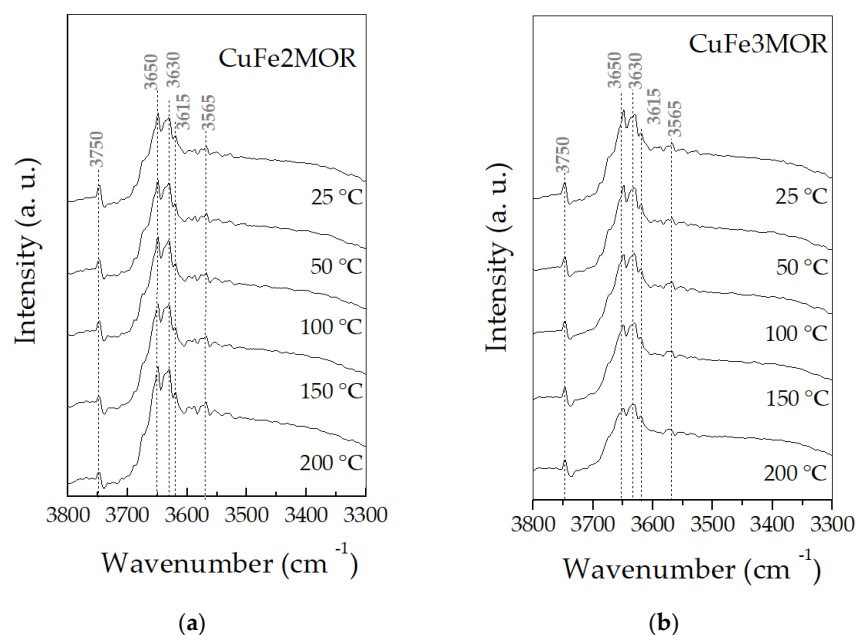


**Figure 3.** DRIFT spectra of hydroxyl region for (a) CuFe2MOR and (b) CuFe3MOR.

Figure 4 shows two optimized configurations for the mordenite zeolite: (a) with only one Fe ion inclusion and (b) with one inclusion of Fe and one inclusion of Cu ions per unit cell. By directly comparing these configurations, it can be seen that, after the introduction of Cu, only minor structural changes occur in the mordenite matrix. This at least reflects the behavior which has been observed for XRD patterns associated with Fe2MOR and CuFe2MOR (see Figure 1). On the other hand, in Figure 4 are shown the most important trends that we observed for exchange cations in the lowest energy configurations: (a) copper cation is located in 8-membered rings, (b) iron is adsorbed in the wall of the main channel (formed by 12-membered ring), and (c) when both Fe and Cu cations are introduced into the unit cell, they tend to be as far apart from each other as possible.

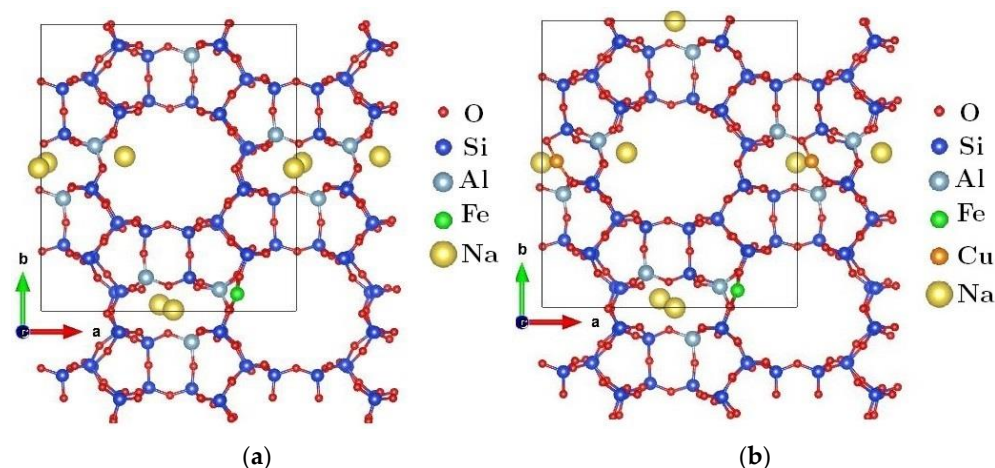


**Figure 4.** Minimal energy configurations for sodic mordenite zeolite with a Si/Al = 7 ratio and: (a) one Fe atom and (b) one Fe and one Cu atom by unit cell. In both cases, the unit cell (delimited by the black square box) was extended to better appreciate atom distribution.

Considering the latter observation, and Cu concentrations reported in Table 1 for the CuMOR and CuFe2MOR samples, it can be assumed that the prior presence of Fe in the zeolite limits the amount of Cu that can enter the NaMOR zeolite. As for Fe adsorption on the main channel wall (Figure 4a,b), upon closer inspection of its local environment, we find

that iron occupies, specifically, a six-membered ring. Figure 5 shows this local structure, in which the Fe atom is almost coplanar to the oxygen atoms, while the immediate Si and Al atoms are outside of this plane. Interestingly, this arrangement of Fe has already been reported for zeolites such as ferrierite, beta, chabazite, faujasite, ZSM-5, and type-A in  $N_2O$  decomposition [31–34], oxidation, and hydrogenation of hydrocarbons [35–37]. Although these studies usually consider a six-membered ring with two aluminums, recent studies on zeolite SSZ-13 show that a ring with a single aluminum more strongly adsorbs a NO molecule [38].

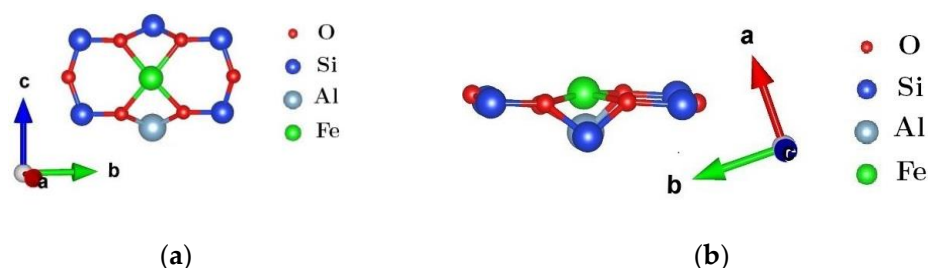


**Figure 5.** Configuration of a Fe atom on a 6-membered ring, shown at two distinct orientations to the crystalline axis of the mordenite unit cell: perpendicular to the a-axis (a) and perpendicular to the c-axis (b).

Figure 6 shows the behavior of the average Löwdin charge, which is represented by various oxygen atoms for each of the different configurations under study. The distinction made here for oxygen atoms refers to the fact that, for mordenite zeolite, there are 10 different non-equivalent positions that they can occupy. On the other hand, the Löwdin charge does not represent a physical charge, but a measure of how occupied the valence orbital of an atom is. This implies that the lower its value, the higher the intrinsic acidity of the atom. Taking the Löwdin charge of oxygen atoms in the NaMOR configuration as a basis, we can conclude that ion exchange with Fe (Fe2MOR configuration) increases the intrinsic acidity of oxygen atoms in the non-equivalent positions I and IV. Inset (a) in Figure 6 demonstrates that these are precisely the type of oxygen with which Fe interacts directly. The introduction of Cu as a second exchange cation (CuFe2MOR configuration) further increases the acidity (primarily) for the non-equivalent sites III and VIII. For the latter case, inset (b) shows that this occurs because these are the type of oxygen atoms with which the Cu cation interacts directly. Thus, compared to the oxygen atoms neighboring Fe, the oxygen atoms in the non-equivalent position VIII present a higher intrinsic acidity because of a higher confinement effect to which they subject the Cu cation. This observation is in agreement with the results of the concentration of surface OH groups. The presence of iron favors the formation of acid sites on the surface, which should have an influence on the performance of the samples for NO reduction via CO oxidation. In this work, only  $Fe^{2+}$  samples were considered since the experimental results for the DRIFT spectra of the hydroxyl region for CuFe2MOR and CuFe3MOR are quite close. Moreover,  $Fe^{3+}$ -containing samples might have an isomorphic substitution of  $Fe^{3+}$  in the crystal lattice, which requires further study.

#### 2.4. Adsorption of Probe Molecules

DRIFT spectroscopy of probe molecules is a very useful method of analysis for obtaining information about the surface and framework sites in zeolites. In order to understand the effect of iron valence on the interactions of CO and NO at the surface, we carried out DRIFT spectroscopy measurements of simultaneously adsorbed CO and NO, up to an equilibrium pressure of about 20 and 10 mbar of CO and NO, respectively (a CO/NO ratio of 2, similar to the catalytic performance procedure). For all of the materials, DRIFT spectra were recorded in the range of CO adsorption ( $2050\text{--}2450\text{ cm}^{-1}$ ). Kostrov et al. proposed a number of distribution ranges for CO adsorption on metals in accordance with



their vibrations:  $M^0\text{-CO}$  ( $\nu_{\text{CO}} \leq 2100 \text{ cm}^{-1}$ ),  $M^+\text{-CO}$  ( $\nu_{\text{CO}} 2120\text{--}2160 \text{ cm}^{-1}$ ), and  $M^{2+}\text{-CO}$  ( $\nu_{\text{CO}} \geq 2170 \text{ cm}^{-1}$ ) [39]. The results of measuring the DRIFT spectra of adsorbed CO are presented in Figure 7a,b. First, the appearance in the spectra of both samples of bands at 2338 and 2361  $\text{cm}^{-1}$ , which correspond to  $\text{CO}_2(\text{g})$ , confirms the idea of CO oxidation to  $\text{CO}_2$  on zeolite-type materials [40]; this could mean that the support has a catalytic activity. For  $\text{CuFe}_3\text{MOR}$  (Figure 7b), these bands are noticeably more intense than for  $\text{CuFe}_2\text{MOR}$  and increase with temperature. This is interesting because it seems that the presence of  $\text{Fe}^{3+}$  is beneficial to the catalytic performance of the samples. Consideration of the individual peaks of each sample is described below.

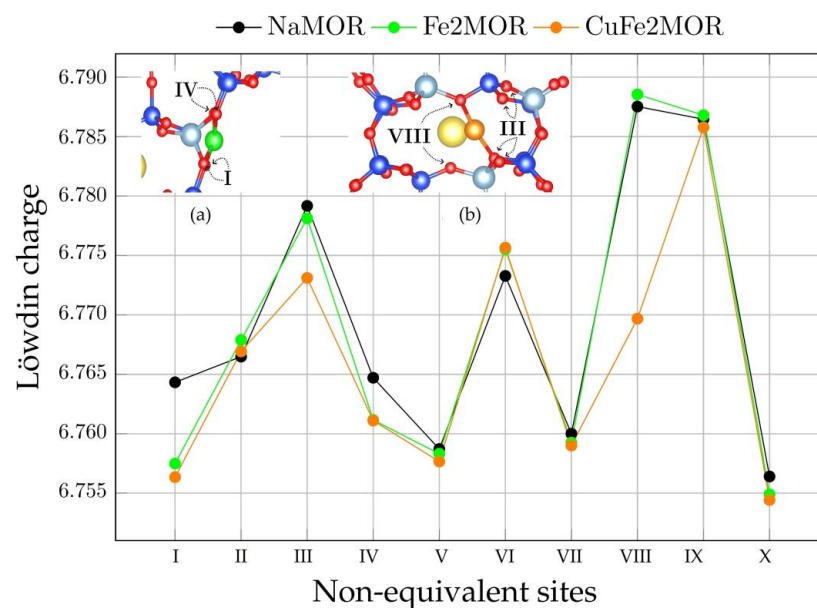


**Figure 6.** Löwdin charge computed for three distinct configurations: NaMOR, Fe2MOR, and CuFe2MOR. Insets (a,b) show the nearest neighbor oxygen atoms (and their respective non-equivalent site) for Fe and Cu cations, respectively.

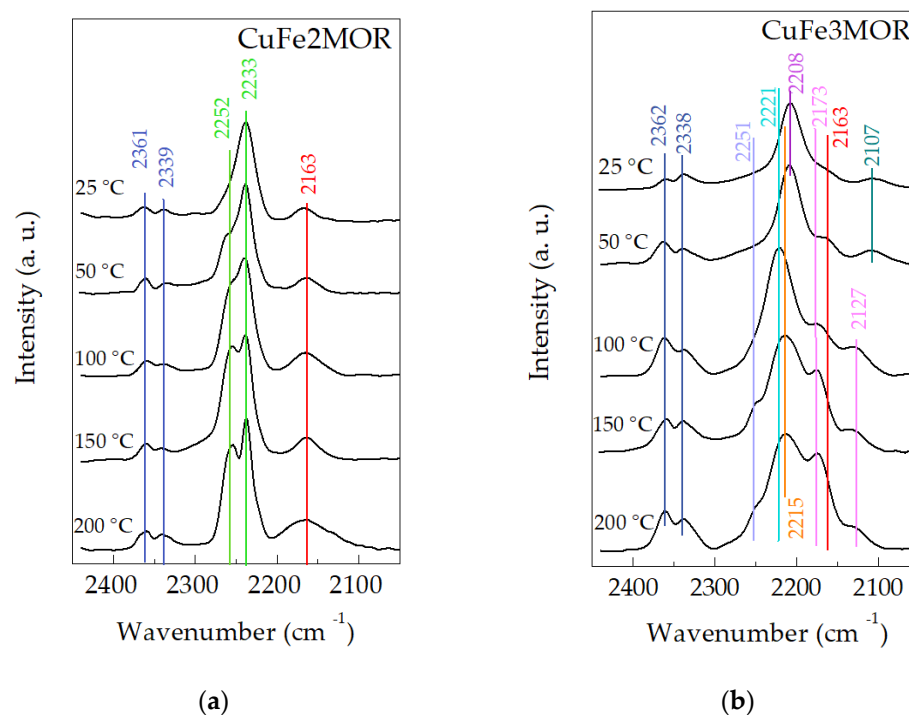


**Figure 7.** DRIFT spectra of adsorbed CO for  $\text{CuFe}_2\text{MOR}$  (a) and  $\text{CuFe}_3\text{MOR}$  (b).

The CuFe2MOR spectra (Figure 7a) show the presence of a band at  $2163\text{ cm}^{-1}$ , which is attributed to the CO-Cu<sup>+</sup> interaction due to the partial reduction in Cu<sup>2+</sup> in the presence of CO. The intensity of the band associated with CO adsorbed on the Cu species drops with the temperature increase. Intense adsorption bands at  $2252$  and  $2233\text{ cm}^{-1}$  correspond to the vibrations of adsorbed N<sub>2</sub>O at the Cu<sup>2+</sup> sites [41,42]. The intensity of these band increases with increasing temperature, which indicates that the interaction of NO with the surface is facilitated with the increase in temperature, which, at higher temperatures, leads to the formation of N<sub>2</sub>, and the oxygen participates in the formation of CO<sub>2</sub>.

The reduction in Cu<sup>2+</sup> by CO is more noticeable for the spectra of CuFe3MOR (Figure 7b). Besides the band at  $2163\text{ cm}^{-1}$ , attributed to CO-Cu<sup>+</sup>, a low-intensity band at  $2107\text{ cm}^{-1}$  appears, which is assigned to the adsorption of CO on Cu<sup>0</sup> at a low temperature. This absorption band disappeared up to  $100\text{ }^{\circ}\text{C}$ , probably due to a Cu<sup>+</sup> reduction into metallic copper species. This is evidenced by a gradual increase in the intensity of the  $2173\text{ cm}^{-1}$  band, as well as the appearance of a new adsorption band at  $2127\text{ cm}^{-1}$ , which are associated with the vibrations of Cu<sup>+</sup>-CO species. Then, there is a reduction in metallic copper species during the reduction of NO via CO oxidation. When CO is adsorbed on the Fe<sup>3+</sup>-zeolite, a band at  $2208\text{ cm}^{-1}$  is observed, which is assigned to the Fe<sup>2+</sup>-CO complexes coming from the reduction in Fe<sup>3+</sup> ions. The band at  $2221\text{ cm}^{-1}$  corresponds to CO adsorbed on Lewis sites (Al<sup>3+</sup>-CO), i.e., the valence of iron affects the surface acidity. The presence of a signal at  $2249\text{ cm}^{-1}$  corresponds to isocyanate complexes. Thus, it can be concluded that the CuFe3MOR surface is more active than the CuFe2MOR surface, which is a beneficial factor for potential catalytic properties.

DRIFT spectra in the region of the adsorbed NO were recorded in the range  $1650\text{--}2000\text{ cm}^{-1}$  (Figure 8). It is remarkable that there is no significant difference in the spectra of CuFe2MOR and CuFe3MOR, except for the intensity of the  $1900\text{ cm}^{-1}$  band which is attributed to the interaction of NO with Cu<sup>2+</sup> ions [43], which is more intense in CuFe2MOR even after high temperature treatment. However, the peak is very broad and can be a summing peak of several bands: Fe<sup>2+</sup>-NO interaction is located at  $1900$  and  $1888\text{ cm}^{-1}$  [44]. On the other hand, it has been reported that NO molecules do not interact with Fe<sup>3+</sup> cations [42], which can explain the difference in adsorption at  $1900\text{ cm}^{-1}$  between CuFe2MOR and CuFe3MOR. A band at  $1860$  and at  $1865\text{ cm}^{-1}$  was noted during the interaction of NO with Cu<sup>2+</sup> in CuO [23,45]. Also, the bands at  $1860\text{ cm}^{-1}$ , together with those at  $1875\text{ cm}^{-1}$ , can be attributed to NO adsorbed on Cu<sup>2+</sup> ions with different effective charges due to different coordination states on the surface [23]. The band located at  $1810\text{ cm}^{-1}$  was attributed to the interaction of NO with Cu<sup>+</sup> ions along the path of nitrosyl species [42]. Absorption at  $1735\text{ cm}^{-1}$  corresponds to the interaction of NO with Cu<sup>+</sup> species, which disappear with a temperature increase. This is in agreement with the DRIFT results of adsorbed CO for CO uptake (Figure 3), which corresponds to the interaction of CO with Cu<sup>+</sup> species [42]. This could be correlated with the interaction of Cu<sup>2+</sup>-NO with some N<sub>2</sub>O species in an adjacent place; therefore, while the intensity of the associated bands decreases with the temperature increase, it allows us to suppose the release of NO<sub>2</sub> or NO<sub>3</sub> species and, consequently, a decrease in the associated bands.

## 2.5. Reduction of NO via CO Oxidation

The results of catalytic activity over CuFe2MOR and CuFe3MOR samples are presented in Figure 9. CuFe3MOR exhibits the best catalytic performance, reaching an NO conversion of 88% at  $150\text{ }^{\circ}\text{C}$ , while the CuFe2MOR only reaches 63% at this temperature. Based on the results of DRIFT for the adsorbed NO and CO, the formation of Cu<sup>+</sup>-NO species was observed. These species are not resistant to temperatures above room temperature but are a mediator for the formation of adsorbed N<sub>2</sub>O, as evidenced by the presence of the absorption band at  $2239\text{ cm}^{-1}$  (Figure 7a). Adsorbed N<sub>2</sub>O can be reduced via interaction with CO molecules that form adsorbed isocyanate complexes (absorption band at  $2253\text{ cm}^{-1}$ , Figure 7a,b), followed by the formation of N<sub>2</sub> and CO<sub>2</sub>. It follows from the DRIFT results that the principal active components are mainly copper oxide sites rather

than Fe species. However, the presence of iron species facilitates the adsorption of NO and CO. Besides, the use of Fe(III) precursor displayed higher catalytic performance in NO reduction via CO oxidation because of the easily reducible intermediate NO-complex adsorbed on the metallic Cu sites, as observed through the in situ DRIFT study. This effect is definitely caused by the interaction between closely contacting Cu and Fe species.

The NO molecule can be reduced by CO into  $N_2O$  and  $N_2$ . Thus, the  $N_2$  selectivity could be calculated as displayed in Figure 9. For all of the catalysts,  $N_2$  selectivity increases as a function of temperature. This was to be expected, since a higher temperature is thermodynamically favorable for further reduction of NO. At temperatures below 110 °C,  $N_2$  selectivity was practically absent. CuFe3MOR exhibits a higher  $N_2$  selectivity in comparison with the CuFe2MOR sample. At temperatures above 110 °C, the CuFe3MOR sample reached 79.3% at 210 °C.  $N_2O$ , as evidenced by the DRIFT results, is an intermediate and product of the NO + CO reaction, principally, up to lower temperatures, while  $N_2$  is likely a direct product at higher temperatures. Then, the nature of the valence of iron also had an important effect on the active species and their selectivity. Thus, both studied samples exhibit catalytic activity; however, CuFe3MOR is more active in NO reduction and more selective to  $N_2$ .

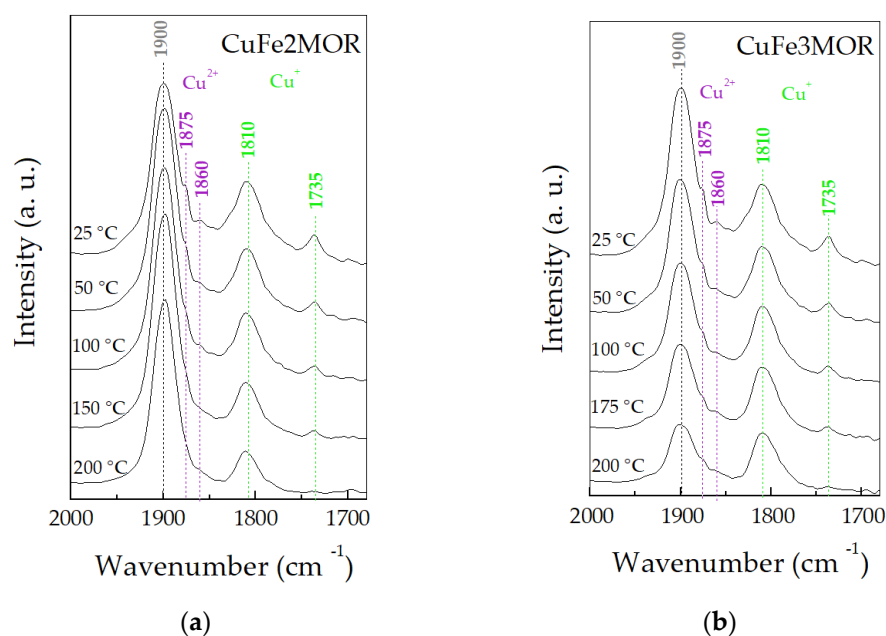


**Figure 8.** DRIFT spectra of adsorbed NO for CuFe2MOR (a) and CuFe3MOR (b).

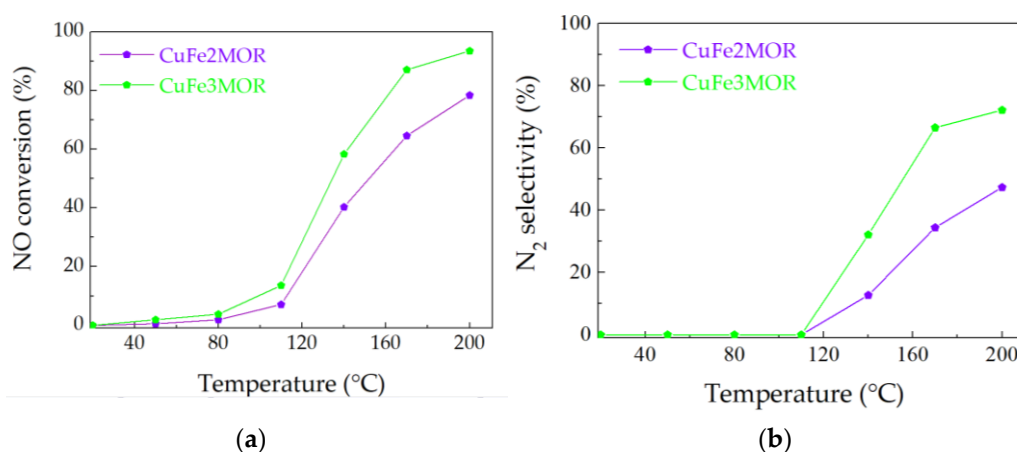


**Figure 9.** NO conversion (a) and selectivity (b) over CuFe2MOR and CuFe3MOR samples.

### 3. Materials and Methods

#### 3.1. Samples Preparation

The sodium form of mordenite (NaMOR) with an atomic ratio of Si/Al = 6.5 was supplied by Zeolyst Int. (Product CBV 10A). The precursor of Cu was 0.5 N CuSO<sub>4</sub> solution, the precursor of Fe<sup>3+</sup> was 0.5 N Fe<sub>2</sub>(SO<sub>4</sub>)<sub>3</sub> solution, and in the case of Fe<sup>2+</sup> it was 0.5 N FeSO<sub>4</sub> solution stabilized against hydrolysis by the addition of H<sub>2</sub>SO<sub>4</sub> until pH = 2 was achieved; this value is based on the data of reference [46]. The ion-exchange solutions preparation parameters are presented in the Table 5. For each sample preparation, NaMOR was treated in a ratio of 1 g/8 mL of liquid, using solutions containing the same total metal equivalent concentration (normality) of both metals. Monometallic samples preparation included one ion exchange step of NaMOR in the appropriate solution. The preparation of bimetallic samples was carried out by ion-exchange from a binary mixture solution at room temperature, when Cu- and Fe-containing solutions were mixed in a volume ratio of 1:1, with a sum concentration of the cations 0.5 N, which were labeled as CuFe2MOR and CuFe3MOR. The metals (Cu and Fe) were introduced to the initial mordenite using the ion exchange method, using 150 MW microwave radiation for 2 h. After the ion exchange procedure, the samples were filtered, washed, and dried at 110 °C for 2 h. Then, they were reduced in a hydrogen flow at a temperature of 350 °C for 1 h followed by cooling and storage in a desiccator with minimal contact with air.

**Table 5.** Ion-exchange solutions preparation parameters.

Sample	Ion Exchange Solution	C <sub>Cu</sub> +C <sub>Fe</sub> in Solution
CuMOR	CuSO <sub>4</sub>	0.5 N of Cu <sup>2+</sup>
Fe2MOR	FeSO <sub>4</sub> , H <sub>2</sub> SO <sub>4</sub> , until pH = 2	0.5 N of Fe <sup>2+</sup>
CuFe2MOR	CuSO <sub>4</sub> , FeSO <sub>4</sub> , H <sub>2</sub> SO <sub>4</sub> until pH = 2	0.5 N, Cu <sup>2+</sup> :Fe <sup>2+</sup> = 1:1
Fe3MOR	Fe <sub>2</sub> (SO <sub>4</sub> ) <sub>3</sub>	0.5 N of Fe <sup>3+</sup>
Cu3FeMOR	CuSO <sub>4</sub> , Fe <sub>2</sub> (SO <sub>4</sub> ) <sub>3</sub>	0.5 N, Cu <sup>2+</sup> :Fe <sup>3+</sup> = 1:1

#### 3.2. Characterization Methods

Quantitative chemical analysis of the samples was carried out by means of the ICP-OES method using a VARIAN VISTA-MPX CCD SIMULTANEOUS spectrometer (Palo Alto, CA, USA). Samples were pretreated by degassing, then dissolved in a mixture of HNO<sub>3</sub> and HF at 40 °C overnight, and a solution of H<sub>3</sub>BO<sub>3</sub> was added at 40 °C for 5 h.

The textural properties were determined from nitrogen adsorption-desorption isotherms at −196 °C, and were recorded with a Micromeritics TriStar 3000 apparatus (Norcross, GA, USA). Before the experiments, the samples were degassed at 300 °C in vacuum for 5 h. The volume of the adsorbed N<sub>2</sub> was normalized to a standard temperature and pressure. The specific surface area (S<sub>BET</sub>) of the samples was calculated by applying the BET method to nitrogen adsorption data within the P/P<sub>0</sub> range of 0.005–0.250. The average pore diameter was calculated by applying the Barret–Joyner–Halenda (BJH) method to the adsorption and desorption branches of the N<sub>2</sub> isotherms. The total pore volume was obtained from isotherms at P/P<sub>0</sub> = 0.99.

High-resolution transmission electron microscopy (HRTEM) studies were carried out using a JEM 2010 microscope (Peabody, MA, USA) operating at an accelerating voltage of 200 kV. The samples were ground into a fine powder and ultrasonically dispersed in isopropanol at room temperature. Then, a drop of the suspension was put on a lace carbon-coated Cu grid. At least 10 representative images were taken for each sample. For each sample, histograms of particle size distribution were plotted, for 450–500 particles on average.

The surface acidity was measured in a fixed bed quartz microflow reactor, using approximately 50 mg of sample over a temperature range of 100–550 °C at a linear heating rate of 10 °C/min. The acidity of the samples was measured by TCD-TPD analysis using a Quantachrome Chem BET Pulsar TPD/TPD (Boynton Beach, FL, USA). First, to remove



moisture, the samples were pre-treated in He (99.99% purity, 120 mL/min, temperature range 100–550 °C, heating rate of 10 °C/min). Then, the samples were kept at 550 °C for 1 h and then cooled down to 100 °C. Anhydrous ammonia with a purity of 99.98% Aldrich (St. Louis, MO, USA) as used for the chemisorption probe at a flow rate of 120 mL/min for 10 min at 100 °C. After that, the adsorbed molecules were removed by applying a flow of He for 40 min.

The DRIFT studies of the adsorbed CO and NO were carried out using an Agilent 660 DRIFT spectrophotometer (Santa Clara, CA, USA) at a resolution of 4 cm<sup>−1</sup> with, a specially designed Praying Mantis diffuse reflection attachment and a low temperature cell (Harrick) for in situ measurements. The samples were pretreated in situ with a N<sub>2</sub> at 400 °C for 1 h, and then degassed at a pressure of 10<sup>−5</sup> mbar for 1 h. Afterwards, the samples were cooled to ambient temperature and exposed to carbon or nitrogen monoxides. The adsorption of CO and NO was performed at room temperature. Small-calibrated doses of CO and NO were introduced in the IR cell up to an equilibrium pressure of approximately 20 and 10 mbar of CO and NO, respectively, after which the temperature was gradually increased and the DRIFT spectra were recorded.

The catalytic activity measurements were conducted in a home-made fixed bed reactor system (12.7 mm I.D.) equipped with a gas analysis unit (DRIFT flue gas analyzer GASMET DX4000, Vantaa, Finland) and a data acquisition system. The modeled gas mixture for the catalytic test was 800 ppm of NO and 1600 ppm of CO balanced by N<sub>2</sub>, using a total flow rate of 100 mL/min, a maintaining a GHSV of 20,000 h<sup>−1</sup>.

#### 4. Conclusions

For the studied bimetallic samples with variable iron valence CuFe2MOR and CuFe3MOR, a high total acidity of both samples was observed. The Brönsted acidity is similar for both samples and is explained by zeolite acidity, and the Lewis acidity varies greatly and depends on the exchange cations. According to TPD data, the acidity of the sample surface also depends on the iron valence. HRTEM confirmed that the valence of iron affects the size distribution of the resulting copper nanoparticles. The charges of iron cations do not have a significant influence on the structure and textural properties of the resulting mordenite materials.

A screening DRIFT study of the spectra of adsorbed CO and NO showed a redox capacity and demonstrated the potential of using these materials as catalysts for ambient protection. CuFe2MOR demonstrated stable Cu and Fe species, while CuFe3MOR showed redox dynamic species. As expected, CuFe3MOR displayed a higher catalytic performance in the NO reduction via CO oxidation, because of the easily reduced intermediate NO-complex which was adsorbed on the metallic Cu and Fe sites, and which were observed through an in situ DRIFT study.

It follows from the DRIFT results that the principal active components are mainly copper oxide sites rather than Fe species. However, the presence of iron species facilitates the adsorption of NO and CO. In addition, the use of Fe(III) precursor displayed a higher catalytic performance in NO reduction via CO oxidation, because of the easily reduced intermediate NO-complex which was adsorbed on the Cu<sup>0</sup> sites. This effect is caused by the interaction between closely contacting Cu and Fe species.

**Supplementary Materials:** The following supporting information can be downloaded at: <https://www.mdpi.com/article/10.3390/catal13030484/s1>, Figure S1: N<sub>2</sub> adsorption/desorption isotherms for samples MOR (a), CuMOR (b), Fe2MOR (c), CuFe2MOR (d), Fe3MOR (e), and CuFe3MOR (f).

**Author Contributions:** Y.K.—conceptualization, investigation, writing—original draft; T.Z.-P.—data curation, formal analysis, investigation, methodology, writing—review & editing; R.Y.-G.—data curation, formal analysis, investigation, methodology, writing—review & editing; J.A.-G.—conceptualization, formal analysis, investigation, methodology, writing—review & editing; L.P.—Data curation, Investigation, Writing—review & editing; M.A.-B.—conceptualization, formal analysis, investigation, writing—review & editing; P.J.V.-S.—Data curation, Formal analysis, Investigation, Writing—review

& editing; S.F.-M.—funding acquisition, project administration, resources, writing—review & editing; V.P.—conceptualization, formal analysis, investigation, writing—original draft, supervision. All authors have read and agreed to the published version of the manuscript.

**Funding:** This research was funded by DGAPA-PAPIIT IG101623 and IN112922, CONACYT, “Basic Science Project A1-S-33492”.

**Data Availability Statement:** The data presented in this study are available on request from the corresponding author.

**Acknowledgments:** The authors thank to M. H. Farías, E. Smolentseva, E. Aparicio-Ceja, J. Mendoza, F. Ruiz, M.A. Estrada, and E. Flores for technical assistance.

**Conflicts of Interest:** The authors declare no conflict of interest.

## References

1. Kwak, J.H.; Tran, D.; Burton, S.D.; Szanyi, J.; Lee, J.H.; Peden, C.H.F. Effects of Hydrothermal Aging on NH<sub>3</sub>-SCR Reaction over Cu/Zeolites. *J. Catal.* **2012**, *287*, 203–209. [\[CrossRef\]](#)
2. Chatterjee, D.; Deutschmann, O.; Warnatz, J. Detailed Surface Reaction Mechanism in a Three-Way Catalyst. *Faraday Discuss.* **2001**, *119*, 371–384. [\[CrossRef\]](#) [\[PubMed\]](#)
3. Shi, Z.; Peng, Q.; Jiaqiang, E.; Xie, B.; Wei, J.; Yin, R.; Fu, G. Mechanism, Performance and Modification Methods for NH<sub>3</sub>-SCR Catalysts: A Review. *Fuel* **2023**, *331*, 125885. [\[CrossRef\]](#)
4. Gramigni, F.; Iacobone, U.; Nasello, N.D.; Sella, T.; Usberti, N.; Nova, I. Review of Hydrocarbon Poisoning and Deactivation Effects on Cu-Zeolite, Fe-Zeolite, and Vanadium-Based Selective Catalytic Reduction Catalysts for NO<sub>x</sub> Removal from Lean Exhausts. *Ind. Eng. Chem. Res.* **2021**, *60*, 6403–6420. [\[CrossRef\]](#)
5. Kubo, T.; Tominaga, H.; Kunugi, T. Oxidation of Carbon Monoxide over Transition Metal Ion-Zeolite Catalysts. *Bull. Chem. Soc. Jpn.* **1973**, *46*, 3549–3552. [\[CrossRef\]](#)
6. Bulánek, R.; Wichterlová, B.; Sobalík, Z.; Tichý, J. Reducibility and Oxidation Activity of Cu Ions in Zeolites. *Appl. Catal. B Environ.* **2001**, *31*, 13–25. [\[CrossRef\]](#)
7. Gao, F.; Zheng, Y.; Kukkadapu, R.K.; Wang, Y.L.; Walter, E.D.; Schwenzer, B.; Szanyi, J.; Peden, C.H.F. Iron Loading Effects in Fe/SSZ-13 NH<sub>3</sub>-SCR Catalysts: Nature of the Fe Ions and Structure–Function Relationships. *ACS Catal.* **2016**, *6*, 2939–2954. [\[CrossRef\]](#)
8. Cheung, T.; Bhargava, S.K.; Hobday, M.; Foger, K. Adsorption of NO on Cu Exchanged Zeolites, an FTIR Study: Effects of Cu Levels, NO Pressure, and Catalyst Pretreatment. *J. Catal.* **1996**, *158*, 301–310. [\[CrossRef\]](#)
9. Metkar, P.S.; Harold, M.P.; Balakotaiah, V. Selective Catalytic Reduction of NO<sub>x</sub> on Combined Fe- and Cu-Zeolite Monolithic Catalysts: Sequential and Dual Layer Configurations. *Appl. Catal. B Environ.* **2012**, *111–112*, 67–80. [\[CrossRef\]](#)
10. Deka, U.; Lezcano-Gonzalez, I.; Weckhuysen, B.M.; Beale, A.M. Local Environment and Nature of Cu Active Sites in Zeolite-Based Catalysts for the Selective Catalytic Reduction of NO<sub>x</sub>. *ACS Catal.* **2013**, *3*, 413–427. [\[CrossRef\]](#)
11. Sazama, P.; Moravkova, J.; Sklenak, S.; Vondrova, A.; Tabor, E.; Sadovska, G.; Pilar, R. Effect of the Nuclearity and Coordination of Cu and Fe Sites in  $\beta$  Zeolites on the Oxidation of Hydrocarbons. *ACS Catal.* **2020**, *10*, 3984–4002. [\[CrossRef\]](#)
12. Bayliss, P.; Kolitsch, U.; Nickel, E.H.; Pring, A. Alunite Supergroup: Recommended Nomenclature. *Mineral. Mag.* **2010**, *74*, 919–927. [\[CrossRef\]](#)
13. Zhukov, Y.M.; Shelyapina, M.G.; Efimov, A.Y.; Zhizhin, E.V.; Petranovskii, V. Recognition of Depth Composition Profiles of Copper-Exchanged Mordenites Applying Analytical Methods with Different Depth Vision. *Mater. Chem. Phys.* **2019**, *236*, 121787. [\[CrossRef\]](#)
14. Bogdanov, D.S.; Novikov, R.G.; Pestov, O.S.; Baranov, D.A.; Shelyapina, M.G.; Tsyganenko, A.A.; Kasatkin, I.A.; Kalganov, V.D.; Silyukov, O.I.; Petranovskii, V. Formation of admixed phase during microwave assisted Cu ion exchange in mordenite. *Mater. Chem. Phys.* **2021**, *261*, 124235. [\[CrossRef\]](#)
15. Shelyapina, M.; Krylova, Zhukov, Y.; Zvereva; Rodriguez-Iznaga, I.; Petranovskii, V.; Fuentes-Moyado, S. Comprehensive Analysis of the Copper Exchange Implemented in Ammonia and Protonated Forms of Mordenite Using Microwave and Conventional Methods. *Molecules* **2019**, *24*, 4216. [\[CrossRef\]](#)
16. Breck, D.W. *Zeolite Molecular Sieves: Structure, Chemistry and Use*; John Wiley & Sons, Inc.: New York, NY, USA, 1974; p. 771.
17. Efimov, A.Y.; Petranovsky, V.P.; Fedotov, M.A.; Khripun, M.K.; Myund, L.A. On the role of triethanolamine in the Charnell synthesis of zeolites. *J. Struct. Chem.* **1993**, *34*, 548–551. [\[CrossRef\]](#)
18. Luo, W.; Yang, X.; Wang, Z.; Huang, W.; Chen, J.; Jiang, W.; Wang, L.; Cheng, X.; Deng, Y.; Zhao, D. Synthesis of ZSM-5 aggregates made of zeolite nanocrystals through a simple solvent-free method. *Microporous Mesoporous Mater.* **2017**, *243*, 112–118. [\[CrossRef\]](#)
19. Matsukata, M.; Osaki, T.; Ogura, M.; Kikuchi, E. Crystallization behavior of zeolite beta during steam-assisted crystallization of dry gel. *Microporous Mesoporous Mater.* **2002**, *56*, 1–10. [\[CrossRef\]](#)
20. Inagaki, S.; Nakatsuyama, K.; Saka, Y.; Kikuchi, E.; Kohara, S.; Matsukata, M. Elucidation of Medium-Range Structure in a Dry Gel-Forming \*BEA-Type Zeolite. *J. Phys. Chem. C* **2007**, *111*, 10285–10293. [\[CrossRef\]](#)
21. Shelyapina, M.G.; Gurgul, J.; Łatka, K.; Sánchez-López, P.; Bogdanov, D.; Kotolevich, Y.; Petranovskii, V.; Fuentes, S. Mechanism of formation of framework Fe<sup>3+</sup> in bimetallic Ag-Fe mordenites-Effective catalytic centers for deNO<sub>x</sub> reaction. *Microporous Mesoporous Mater.* **2019**, *299*, 109841. [\[CrossRef\]](#)

22. Chen, L.; Janssens, T.V.W.; Skoglundh, M.; Grönbeck, H. Interpretation of NH<sub>3</sub>-TPD Profiles from Cu-CHA Using First-Principles Calculations. *Top. Catal.* **2018**, *62*, 93–99. [\[CrossRef\]](#)
23. Benaliouche, F.; Boucheffa, Y.; Ayrault, P.; Mignard, S.; Magnoux, P. NH<sub>3</sub>-TPD and FTIR Spectroscopy of Pyridine Adsorption Studies for Characterization of Ag- and Cu-Exchanged X Zeolites. *Microporous Mesoporous Mater.* **2008**, *111*, 80–88. [\[CrossRef\]](#)
24. Davydov, A. The Nature of Oxide Surface Centers. In *Molecular Spectroscopy of Oxide Catalyst Surfaces*; John Wiley & Sons, Inc.: Hoboken, NJ, USA, 2003; pp. 27–179.
25. Marie, O.; Massiani, P.; Thibault-Starzyk, F. Infrared evidence of a third brønsted site in mordenites. *J. Phys. Chem. B* **2004**, *108*, 5073–5081. [\[CrossRef\]](#)
26. Makarova, M.A.; Wilson, A.E.; Van Liemt, B.J.; Mesters, C.M.; De Winter, A.M.; Williams, C. Quantification of Brønsted acidity in mordenites. *J. Catal.* **1997**, *172*, 170–177. [\[CrossRef\]](#)
27. Jiang, M.; Karge, H.G. Investigation of acid properties of dealuminated H-mordenite zeolites by low-temperature diffuse reflectance FTIR. *J. Chem. Soc. Faraday Trans.* **1996**, *92*, 2641–2649. [\[CrossRef\]](#)
28. Wu, P.; Komatsu, T.; Yashima, T. Isomorphous substitution of Fe<sup>3+</sup> in the framework of aluminosilicate mordenite by hydrothermal synthesis. *Microporous Mesoporous Mater.* **1998**, *20*, 139–147. [\[CrossRef\]](#)
29. Bevilacqua, M.; Busca, G. A study of the localization and accessibility of Brønsted and Lewis acid sites of H-mordenite through the FT-IR spectroscopy of adsorbed branched nitriles. *Catal. Commun.* **2002**, *3*, 497–502. [\[CrossRef\]](#)
30. Antúñez-García, J.; Galván, D.H.; Petranovskii, V.; Murrieta-Rico, F.N.; Yocupicio-Gaxiola, R.I.; Shelyapina, M.G.; Fuentes-Moyado, S. Aluminum Distribution in Mordenite-Zeolite Framework: A New Outlook Based on Density Functional Theory Calculations. *J. Solid State Chem.* **2022**, *306*, 122725. [\[CrossRef\]](#)
31. Sobalík, Z.; Tvarůžková, Z.; Vondrová, A.; Schwarze, M. Targeted Preparation of Fe-Zeolites with Iron Prevailing in Extraframework Cationic Positions. *Stud. Surf. Sci. Catal.* **2006**, *162*, 889–896.
32. Sklenak, S.; Andrikopoulos, P.C.; Boekfa, B.; Jansang, B.; Nováková, J.; Benco, L.; Bucko, T.; Hafner, J.; Dědeček, J.; Sobalík, Z. N<sub>2</sub>O Decomposition over Fe-Zeolites: Structure of the Active Sites and the Origin of the Distinct Reactivity of Fe-Ferrierite, Fe-ZSM-5, and Fe-Beta. A Combined Periodic DFT and Multispectral Study. *J. Catal.* **2010**, *272*, 262–274. [\[CrossRef\]](#)
33. Bols, M.L.; Hallaert, S.D.; Snyder, B.E.R.; Devos, J.; Plessers, D.; Rhoda, H.M.; Dusselier, M.; Schoonheydt, R.A.; Pierloot, K.; Solomon, E.I.; et al. Spectroscopic Identification of the  $\alpha$ -Fe/ $\alpha$ -O Active Site in Fe-CHA Zeolite for the Low-Temperature Activation of the Methane C–H Bond. *J. Am. Chem. Soc.* **2018**, *140*, 12021–12032. [\[CrossRef\]](#) [\[PubMed\]](#)
34. Daouli, A.; Hessou, E.P.; Monnier, H.; Dziurla, M.-A.; Hasnaoui, A.; Maurin, G.; Badawi, M. Adsorption of NO, NO<sub>2</sub> and H<sub>2</sub>O in Divalent Cation Faujasite Type Zeolites: A Density Functional Theory Screening Approach. *Phys. Chem. Chem. Phys.* **2022**, *24*, 15565–15578. [\[CrossRef\]](#) [\[PubMed\]](#)
35. Snyder, B.E.R.; Vanelderen, P.; Bols, M.L.; Hallaert, S.D.; Böttger, L.H.; Ungur, L.; Pierloot, K.; Schoonheydt, R.A.; Sels, B.F.; Solomon, E.I. The Active Site of Low-Temperature Methane Hydroxylation in Iron-Containing Zeolites. *Nature* **2016**, *536*, 317–321. [\[CrossRef\]](#) [\[PubMed\]](#)
36. Devos, J.; Bols, M.L.; Plessers, D.; Goethem, C.V.; Seo, J.W.; Hwang, S.-J.; Sels, B.F.; Dusselier, M. Synthesis–Structure–Activity Relations in Fe-CHA for C–H Activation: Control of Al Distribution by Interzeolite Conversion. *Chem. Mater.* **2019**, *32*, 273–285. [\[CrossRef\]](#)
37. Bols, M.L.; Snyder, B.E.R.; Rhoda, H.M.; Cnudde, P.; Fayad, G.; Schoonheydt, R.A.; Van Speybroeck, V.; Solomon, E.I.; Sels, B.F. Coordination and Activation of Nitrous Oxide by Iron Zeolites. *Nat. Catal.* **2021**, *4*, 332–340. [\[CrossRef\]](#)
38. Mesilov, V.; Pon, L.; Dahlin, S.; Bergman, S.L.; Pettersson, L.J.; Bernasek, S.L. Computational Study of Noble Metal CHA Zeolites: NO Adsorption and Sulfur Resistance. *J. Phys. Chem. C* **2022**, *126*, 7022–7035. [\[CrossRef\]](#)
39. Kostrov, V.V.; Lokhov, Y.; Morozov, L.N.; Davydov, A. Study of the state of transition-metal cations on catalyst surfaces by IR spectroscopy of adsorbed test molecules (CO, NO). 3. Copper-aluminum catalysts (CuO–Al<sub>2</sub>O<sub>3</sub>). *Kinet. Catal.* **1980**, *21*, 943–946.
40. Adak, S.; Pal, R.S.; Khan, T.S.; Poddar, M.K.; Ahmad, M.S.; Prasad, V.V.; Haider, M.A.; Bal, R. Role of Interfacial Cu-Ions in Polycrystalline Cu–CeO<sub>2</sub>: In-Situ Raman, In-situ DRIFT and DFT Studies for Preferential Oxidation of CO in Presence of Excess H<sub>2</sub>. *ChemistrySelect* **2021**, *6*, 13051–13059. [\[CrossRef\]](#)
41. Szanyi, J.; Kwak, J.H.; Zhu, H.; Peden, C.H.F. Characterization of Cu-SSZ-13 NH<sub>3</sub> SCR Catalysts: An in Situ FTIR Study. *Phys. Chem. Chem. Phys.* **2013**, *15*, 2368. [\[CrossRef\]](#)
42. Ramírez-Garza, R.E.; Rodríguez-Iznaga, I.; Simakov, A.; Farías, M.H.; Castellón-Barraza, F.F. Cu–Ag/Mordenite Catalysts for NO Reduction: Effect of Silver on Catalytic Activity and Hydrothermal Stability. *Mater. Res. Bull.* **2018**, *97*, 369–378. [\[CrossRef\]](#)
43. Davydov, A. Study of Cation States by DRES and FTIR Spectroscopies of the Probe Molecules. In *Molecular Spectroscopy of Oxide Catalyst Surfaces*; John Wiley & Sons, Inc.: Hoboken, NJ, USA, 2003; pp. 181–275.
44. Gao, F. Fe-Exchanged Small-Pore Zeolites as Ammonia Selective Catalytic Reduction (NH<sub>3</sub>-SCR) Catalysts. *Catalysts* **2020**, *10*, 1324. [\[CrossRef\]](#)
45. Kuterasiński, L.; Podobiński, J.; Madej, E.; Smoliło-Utrata, M.; Rutkowska-Zbik, D.; Datka, J. Reduction and oxidation of Cu species in Cu-faujasites studied by IR spectroscopy. *Molecules* **2020**, *25*, 4765. [\[CrossRef\]](#) [\[PubMed\]](#)
46. Brandenberger, S.; Kröcher, O.; Tissler, A.; Althoff, R. The State of the Art in Selective Catalytic Reduction of NO<sub>x</sub> by Ammonia Using Metal-Exchanged Zeolite Catalysts. *Catal. Rev.* **2008**, *50*, 492–531. [\[CrossRef\]](#)

**Disclaimer/Publisher’s Note:** The statements, opinions and data contained in all publications are solely those of the individual author(s) and contributor(s) and not of MDPI and/or the editor(s). MDPI and/or the editor(s) disclaim responsibility for any injury to people or property resulting from any ideas, methods, instructions or products referred to in the content.